 CMC, vol.4, no.1, pp.43-53, 2006

Computational Modeling of Impact Response with the RG Damage Model and the Meshless Local Petrov-Galerkin (MLPG) Approaches

H. T. Liu[1], Z. D. Han[1], A. M. Rajendran[2], S. N. Atluri[3]

Abstract: The Rajendran-Grove (RG) ceramic damage model is a three-dimensional internal variable based constitutive model for ceramic materials, with the considerations of micro-crack extension and void collapse. In the present paper, the RG ceramic model is implemented into the newly developed computational framework based on the Meshless Local Petrov-Galerkin (MLPG) method, for solving high-speed impact and penetration problems. The ability of the RG model to describe the internal damage evolution and the effective material response is investigated. Several numerical examples are presented, including the rod-on-rod impact, plate-on-plate impact, and ballistic penetration. The computational results are compared with available experiments, as well as those obtained by the popular finite element code (Dyna3D).

keyword: Rajendran-Grove ceramic model, Material modeling, Ceramic damage, Meshless method, MLPG, High-speed impact, Penetration and perforation

1 Introduction

Ceramic materials are an important category of materials that have been widely used in armor elements, engine turbine blades and other structural components, because of their enhanced dynamic compressive strength and high temperature properties. Accurately modeling the constitutive behavior of ceramics, including their damage and failure, is essential in the device-design, and their deployment for dynamic structural and armor applications. Recently, Rajendran and Grove (Rajendran, 1994; Rajendran and Grove, 1996) proposed a three-dimensional, internal state variable based constitutive model (RG ceramic damage model) for ceramic materials, which incorporated both micro-crack propagation and void collapse. The proposed RG ceramic damage model has been implemented into EPIC code for investigating the model's ability to describe the response of pure alumina (AD995) subjected to various stress/strain loading conditions (Rajendran and Grove, 2002).

In the present paper, the RG ceramic damage model is implemented into the newly developed computational code based on the Meshless Local Petrov-Galerkin (MLPG) method. The MLPG method is a truly meshless approach that establishes both the trial and test functions in local subdomains. Because of the total elimination of the mesh, it is a promising method in solving high-speed contact, impact and penetration problems with severe material-distortion. The detailed description of the MLPG and its applications can be found in the authors' other papers. For comparison and verification purpose, the RG model has also been implemented into the three-dimensional computational hydrodynamic code Dyna3D. Several numerical examples are solved, using either the Dyna3D or the MLPG method, with RG ceramic damage model implemented in them. Several numerical simulations are conducted: rod-on-rod impact, plate-on-plate impact, and the ballistic impact and penetration. The simulation results obtained from Dyna3D, MLPG and available experiments are compared. For completeness purpose, a brief introduction of the RG ceramic damage model is included.

2 Rajendran-Grove Ceramic Damage Model

In the Rajendran-Gove ceramic model, the following assumptions are made: 1) randomly distributed and oriented micro-cracks are pre-existing in the materials, 2) plastic flow occurs when the materials are shocked above the HEL (Hugoniot Elastic Limit), 3) pore collapse is due to the plastic flow in the matrix surrounding the pores, 4) no plastic flow happens when the material is under tensile loading, 5) micro-cracks propagate under both compression and tension, and 6) pulverization occurs under compressive loading, when the accumulated micro-crack density reaches a critical value. The micro-crack dam-

[1] Knowledge Systems Research, LLC, Forsyth, GA 30253
[2] US Army Research Office (ARO), RTP, NC
[3] Center for Aerospace Research & Education, University of California, Irvine

age is described using a dimensionless damage density parameter in terms of the maximum micro-crack size and the average number of micro-cracks per unit volume. The damage evolution in terms of crack growth is formulated based on a generalized Griffith criterion (Griffith, 1920). The stiffness reduction due to micro-cracking is modeled using the analytical formulation from Margolin (1983) and Budiansky and O'Connell (1976). The pore collapse effects are modeled using viscoplastic equations derived from Gurson's pressure dependent yield function (Gurson, 1977). In the following sections, the Rajendran-Grove ceramic model is briefly reviewed.

2.1 Constitutive Relationships

The total strain $\varepsilon_{ij}$is decomposed into the elastic part ε^e_{ij} and plastic part ε^p_{ij} as

$$\varepsilon_{ij} = \varepsilon^e_{ij} + \varepsilon^p_{ij} \tag{1}$$

Here, the elastic strain includes the elastic strain of the intact matrix material and the strain due to micro-crack opening/sliding. The plastic strain is associated with pore collapse and occurs only when the applied pressure exceeds the pressure at the Hugoniot Elastic Limit (HEL). The total stress σ_{ij} is decomposed into deviatoric stress S_{ij} and pressure P as

$$\sigma_{ij} = S_{ij} - P\delta_{ij} \tag{2}$$

The pressure is calculated through the Mie-Gruneisen equation of state which given by

$$P = \left[\overline{P}_H\left(1 - 0.5\Gamma\overline{\eta}\right) + \Gamma\rho_0\left(I - I_0\right)\right] \tag{3}$$

where

$$\overline{P}_H = K_\gamma\left(\beta_1\overline{\eta} + \beta_2\overline{\eta}^2 + \beta_3\overline{\eta}^3\right) \tag{4}$$

In the above equations, β_1, β_2 and β_3 are empirical parameters; Γ is the Mie-Gruneisen parameter; $K_\gamma = \overline{K}/K$ is the bulk modulus reduction ratio with K the bulk modulus for the intact matrix and $\overline{K}$ the effective bulk modulus for the micro-crack containing material (Margolin, 1983; Budiansk and O'Connell 1976). Furthermore, ρ_0 is the initial material density; I_0 and I are the internal energy at the initial and current states, respectively. The engineering volumetric strain, with the consideration of the voids, is defined as

$$\overline{\eta} = \frac{(1-f_0)V_0}{(1-f)V} - 1 \tag{5}$$

Where V_0 and V are the volumes of the initial and current states; f_0 and f are the initial and current porosity densities, respectively.

The deviatoric stress is related to the deviatoric elastic strain e^e_{ij}, as

$$S_{ij} = 2R_g\overline{G}e^e_{ij} \tag{6}$$

Here $\overline{G}$ is the effective shear modulus for micro-crack containing material (Margolin, 1983; Budiansky and O'Connell, 1976) and R_g is the correction factor for shear modulus due to the existence of porosity, which is expressed as

$$R_g = (1-f)\left[1 - \frac{(6K+12G)f}{(9K+8G)}\right] \tag{7}$$

with G the shear modulus for the intact matrix. The porosity density is assumed to decrease, due to void collapsing at pressures above the HEL, as

$$\dot{f} = (1-f)\dot{\varepsilon}^p_v \tag{8}$$

where ε^p_v the plastic volumetric strain, and the dot above a symbol implies the temporal derivative.

When the materials are shocked above the HEL (Hugoniot Elastic Limit), plastic flow occurs. In the current model, Gurson's pressure dependent yield function (Gurson, 1977) when considerations of the porosity are included, namely

$$F = \frac{3J_2}{Y^2} + 2f\cosh\left(\frac{3P}{2Y}\right) - f^2 - 1 = 0 \tag{9}$$

with $J_2 = 0.5S_{ij}S_{ij}$. A simplified Johnson-Cook strain rate dependent strength model (Johnson and Cook, 1985) is used and can be expressed as

$$Y = C_1\left(1 + C_3\ln\frac{\dot{\varepsilon}_p}{\dot{\varepsilon}_0}\right) \tag{10}$$

where C_1 and C_3 are model constants. $\dot{\varepsilon}_p$ is the equivalent plastic strain rate and $\dot{\varepsilon}_0$ is the reference strain rate, which is assumed to be 1 in the current model.

Figure 1 qualitatively shows the effect of the void collapse on the material response under a hydrostatic loading/unloading condition predicted by the RG model. With the increase of the compressive hydrostatic loading, the voids start to collapse at point **A**. At point **B**, the volume of the voids reduces to zero and the corresponding porosity f becomes 0. During the unloading process, at point **C**, the pressure reduces to zero, but the volumetric strain does not go to zero due to the collapsed void volume.

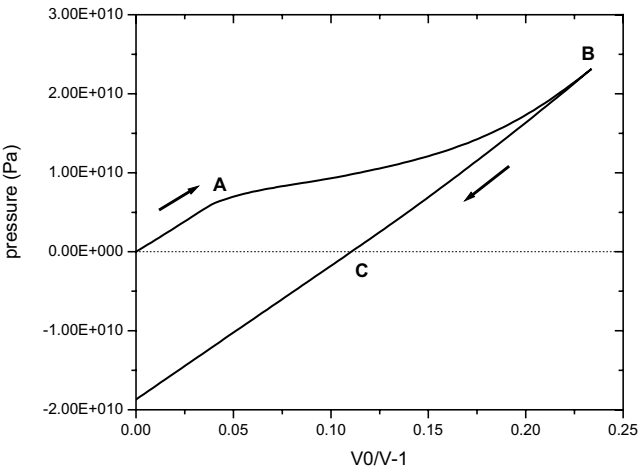

Figure 1 : The hydrostatic loading/unloading of RG model with void collapse

2.2 Damage Definition and Evolution

The micro-crack damage is measured in terms of a dimensionless micro-crack damage density γ, which is expressed as

$$\gamma = N_0^* a^3 \tag{11}$$

where N_0^* is the average number of micro-flaws per unit volume, and a is the maximum micro-crack size at the current state. The initial values of N_0^* and a_0 are material constants. For simplicity, it is assumed that no cracks nucleate during the loading, and therefore the damage evolution is represented by the growth of micro-crack size a, which follows a generalized Griffith criterion (Griffith, 1920) as

$$\dot{a} = \begin{cases} 0 & ,G_s \le G_C \\ n_1 C_R \left[1 - \left(\frac{G_C}{G_S}\right)^{n_2}\right] & G_s > G_C \end{cases} \tag{12}$$

where C_R is the Rayleigh wave speed, G_C is the critical strain energy release rate for micro-crack growth calculated from the fracture toughness K_{IC}, Young's modulus E and Poisson's ratio v as $G_C = K_{IC}^2\left(1-v^2\right)/E$. G_S is the applied strain energy release rate. n_1 and n_2 are the parameters controlling the crack growth rate. Four parameters are used for the micro-crack extension model: n_1^- and n_2^- for crack sliding, and n_1^+ and n_2^+ for crack opening. The applied strain energy release rates are calculated in the principal directions, with $\sigma_1, \sigma_2, \sigma_3$ being the three principal stress components. For crack opening

$$G_S^+ = \frac{4\left(1-v^2\right)}{\pi E} \max\left(0, \sigma_1, \sigma_2, \sigma_3\right)^2 \tag{13}$$

and for crack sliding

$$G_S^- = \max\left(G_1^-, G_2^-, G_3^-\right) \tag{14}$$

with

$$G_i^- = \frac{8\left(1-v^2\right)a}{\pi E\left(2-v\right)} \left\{ \frac{\left|\sigma_j - \sigma_k\right|}{2} + \min\left[0, \mu\frac{\sigma_j+\sigma_k}{2}\right] \right\}^2 \tag{15}$$

In the above equation, $i, j, k = 1, 2, 3$ and $i \neq j \neq k$. μ is the dynamic friction coefficient.

As an example, we show the shear loading response with micro-crack evolution predicted by the RG model in Figure 2. With the increase of the applied shear loading, the strain energy release rate goes beyond the critical energy release rate at the point **A**, activating the micro-cracks sliding. The micro-crack damage density γ increases proportional to the growth of the micro-crack size and the effective shear modulus in Eq. (6) decreases. Therefore, a softening stage corresponding to the micro-cracks extension is form in this figure between point **A** and **B**.

2.3 Pulverization

When the micro-crack damage density γ reaches a critical value (usually set as 0.75) under compressive loading, the material becomes pulverized. The bulk and shear moduli for the pulverized material are set to the corresponding effective bulk and shear moduli at the pulverization point as

$$\overline{K}_p = \overline{K},\ \overline{G}_p = \overline{G} \tag{16}$$

The pulverized material does not support any tensile loading and the compressive strength of the pulverized

material is described by the Mohr-Columb law as

$$Y = \begin{cases} 0 & ,P \le 0 \\ \alpha + \beta P & ,P > 0 \end{cases} \tag{17}$$

where α and β are model constants. The pressure is simply computed from the elastic volumetric strain ε_v^e as

$$P = \begin{cases} 0 & ,\varepsilon_v^e \ge 0 \\ -\overline{K}_p \varepsilon_v^e & \varepsilon_v^e < 0 \end{cases} \tag{18}$$

2.4 Determination of Model Constants

In the Rajendran-Grove ceramic model, there are eight material constants to describe the micro-crack behavior: N_0^*, a_0, μ, n_1^+, n_2^+, n_1^-, n_2^-, and K_{IC}. Usually, several experiments like plate-on-plate and bar-on-bar impact tests are needed to determine these constants for a specific material. Rajendran and Grove (1996) conducted a sensitivity study of the material constants and calibrated the constants for several commonly used ceramic materials, like SiC, B_4C, TiB_2, AD85, and AD995 (Rajendran and Grove, 1996 and 2002; Grove, 1993). In the following numerical simulations, the AD995 and AD85 ceramic are used and the material constants that we employed are listed in Table 1.

3 Meshless Local Petrov-Galerkin Method

Meshless Local Petrov-Galerkin Method (MLPG) [Atluri and Zhu (1998), and Atluri (2004)] is a truly meshless approach, in which both the trial and test functions are established in local subdomains. As an extension to the primitive MLPG method, Atluri Han, and Rajendran proposed an MLPG mixed method to simplify the formulation and improve the efficiency and stability of the MLPG approach [Atluri, Han and Rajendran (2004), Han, Rajendran and Atluri (2005)]. In this MLPG mixed method, both displacement/velocity gradients and displacements/velocities are interpolated independently. Their compatibility is enforced only at the nodal points. Therefore, the continuity requirement of the trial function is reduced by one order, and the second derivatives of the shape functions are eliminated. This MLPG mixed method has been implemented to solve static problems with large deformation [Atluri, Han and Rajendran (2004)] and dynamic problems [Han, Rajendran and Atluri (2005)]. Recently, the authors have successfully applied the MLPG mixed method to solve three-dimensional high-speed contact and impact problems with large deformation [Han, Liu, Rajendran, and atluri (2006)].

In this section, a brief introduction of the MLPG mixed method is presented. Interested readers are encouraged to refer to the above mentioned MLPG papers for detailed formulations.

3.1 Local Nodal Interpolation

In the current implementation, the Moving Least Squares (MLS) is adopted as the local nodal interpolation scheme because of the reasonable accuracy, completeness, robustness and continuity of the MLS functions With the MLS, a trail function $u(\mathbf{x})$ can be expressed as

$$u(\mathbf{x}) = \sum_{I=1}^{N} \Phi^I(\mathbf{x}) \hat{u}^I \tag{19}$$

where $\hat{u}^I$ and $\Phi^I(\mathbf{x})$ are the fictitious nodal value and shape function of node I, respectively. The shape functions are obtained by minimizing the L_2 norm of the weighted distance between the trial function value and its true values at nodal points. The explicit expressions for the shape functions can be found in Atluri (2004).

In the mixed method, we interpolate the velocities v_i, and the velocity gradients $v_{i,j}$, independently, using the same shape functions, namely

$$v_i(\mathbf{x}) = \sum_{J=1}^{N} \Phi^J(\mathbf{x}) v_i^J \tag{20}$$

$$v_{i,j}(\mathbf{x}) = \sum_{K=1}^{N} \Phi^K(\mathbf{x}) v_{i,j}^K \tag{21}$$

The compatibility condition between the velocities and velocity gradients is enforced only at the nodes by a standard collocation method, as

$$v_{i,j}(\mathbf{x}^I) = \frac{\partial v_i(\mathbf{x}^I)}{\partial x_j} \tag{22}$$

By interpolating the velocity gradients, as one of the key features of the mixed method, we eliminate the differentiation operations of the shape functions in the local weak form integration. Therefore, the requirement of the completeness and continuity of the shape functions

Table 1 : The material constants for Rajendran-Grove model

	AD995	AD85
Density (g/cm^3)	3.89	3.42
Shear Modulus (GPa)	156	88.0
Initial Porosity	0	10%
Material Strength Constants		
C_1 (GPa)	2.3	4.0
C_3	0.2	0.029
Equation of State Constants		
β_1 (GPa)	231	150.0
β_2 (GPa)	-169	150.0
β_3 (GPa)	2774	150.0
Γ	0.1	0
Damage Model Parameters		
N_0^* (m^{-3})	2×10^{11}	1.83×10^{10}
a_0 (μm)	20	0.58
μ	0.45	0.72
n_1^+	1.0	1.0
n_2^+	1.0	0.07
n_1^-	0.1	0.1
n_2^-	1.0	0.07
K_{IC} ($MPa\sqrt{m}$)	3.0	3.25
Pulverized Material Constants		
α (GPa)	0	0.1
β	1.0	0.1

is reduced by one-order, and thus, lower-order polynomial terms can be used in the meshless approximations. This leads to a smaller nodal influence size and speeds up the calculation of the shape functions. The adoption of the mixed method in our implementation greatly improves the program efficiency.

3.2 Formulations for Finite Strain Problems

We adopted an updated Lagrangian formulation in our implementation for solving the high-speed dynamic problems. Let x_i be the spatial coordinates of a material particle in the current configuration. Let $\dot{S}_{ij}$ be the Truesdell stress-rate (the rate of second Piola-Kirchhoff stress as referred to the current configuration); and let $\dot{\sigma}^J_{ij}$ be the Jaumann rate of Kirchhoff stress (which is J times the Cauchy stress, where J is the ratio of volumes). It is known [Atluri (1980)]:

$$\dot{S}_{ij} = \dot{\sigma}^J_{ij} - D_{ik}\sigma_{kj} - \sigma_{ik}D_{kj} \tag{23}$$

Here, D_{ij} and W_{ij} are the symmetric and skew-symmetric parts of the velocity gradient, respectively. Considering a 3D domain Ω with a boundary $\partial\Omega$, the rate forms of the linear and angular momentum balances are [Atluri (1980)]:

$$(\dot{S}_{ij} + \tau_{ik}v_{j,k})_{,i} + \dot{f}_j = \dot{b}_j \tag{24}$$

where, $\dot{b}_j = \rho\dot{a}_j$ is the inertia force rate with ρ is the mass density and $\dot{a}_j$ the acceleration rate. In a dynamic problem, $\dot{f}_j$ are appropriately defined in terms of the rate of change of inertia forces and $(\,)_{,i} = \partial(\,)/\partial x_i$; x_i are current coordinates of a material particle. In Eq. (24), τ_{ij} is the Cauchy stress in the current configuration.

3.3 Local weak form with the large deformations

In the MLPG approaches, the weak form is established over a local subdomain Ω_s, which may have an arbitrary shape, and contain a point $\mathbf{x}$ in question. In our implementation, the local weak form is established for a spherical subdomain with the radius of r (we define it as the test-function size), namely

$$\int_{\Omega_s} [(\dot{S}_{ij} + \tau_{ik} v_{j,k})_{,i} + \dot{f}_j - \dot{b}_j] w_j d\Omega = 0 \tag{25}$$

where w_j are the test functions. By applying the divergence theorem, Eq. (25) may be rewritten in a symmetric weak form, as:

$$\int_{\partial\Omega_s} (\dot{S}_{ij} + \tau_{ik} v_{j,k}) n_i w_j d\Gamma - \int_{\Omega_s} [(\dot{S}_{ij} + \tau_{ik} v_{j,k}) w_{j,i} - \dot{f}_j w_j + \dot{b}_j] d\Omega = 0 \tag{26}$$

wherein, the rate definition $\dot{t}_j = (\dot{S}_{ij} + \tau_{ik} v_{j,k}) n_i$, with n_i being the components of a unit outward normal to the boundary of the local subdomain Ω_s, in its current configuration, is used. Thus the local symmetric weak form can be rewritten as

$$\int_{L_s} \dot{t}_i w_i d\Gamma + \int_{\Gamma_{su}} \dot{t}_i w_i d\Gamma + \int_{\Gamma_{st}} \dot{\bar{t}}_i w_i d\Gamma - \int_{\Omega_s} [(\dot{S}_{ij} + \tau_{ik} v_{j,k}) w_{j,i} - \dot{f}_i w_i + \dot{b}_j) d\Omega = 0 \tag{27}$$

where Γ_{su} is a part of the boundary $\partial\Omega_s$ of Ω_s, over which the essential boundary conditions are specified. In general, $\partial\Omega_s = \Gamma_s \cup L_s$, with Γ_s being a part of the local boundary located on the global boundary, and L_s is the other part of the local boundary which is inside the solution domain. $\Gamma_{su} = \Gamma_s \cap \Gamma_u$ is the intersection between the local boundary $\partial\Omega_s$ and the global displacement boundary Γ_u; $\Gamma_{st} = \Gamma_s \cap \Gamma_t$ is a part of the boundary over which the natural boundary conditions are specified.

To simplify the integration and speed up the numerical implementation, the Heaviside function is adopted as the test function in our program. Thus, the local symmetric weak form in Eq.(27) becomes

$$-\int_{L_s} \dot{t}_i d\Gamma - \int_{\Gamma_{su}} \dot{t}_i d\Gamma + \int_{\Omega_s} \dot{b}_j d\Omega = \int_{\Gamma_{st}} \dot{\bar{t}}_i d\Gamma + \int_{\Omega_s} \dot{f}_i d\Omega \tag{28}$$

4 Numerical Simulations

For the implementation of the Rajendran-Grove ceramic damage model, a material subroutine is developed. To maintain the stability of the explicit algorithm, an iterative scheme based on a second-order diagonally implicit Runge-Kutta method is employed to solve the coupled differential equations of the constitutive model. This material subroutine is linked to the Dyna3D (2000 version) hydrodynamic code and the newly developed MLPG mixed program. Numerical examples are conducted either under the Dyna3D (finite element method) and the meshless method (MLPG).

4.1 Beam Under Stretch and Rotation

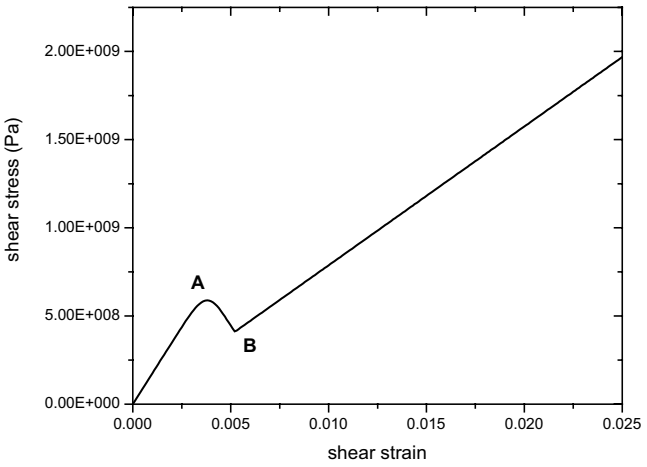

Figure 2 : The shear loading response of RG model with micro-crack evolution

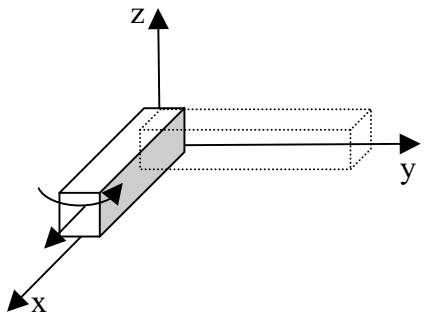

Figure 3 : A beam under stretch and rotation

In the first example, we consider a beam undertaking a uniaxial stretch in the x-direction, as shown in Figure 3.

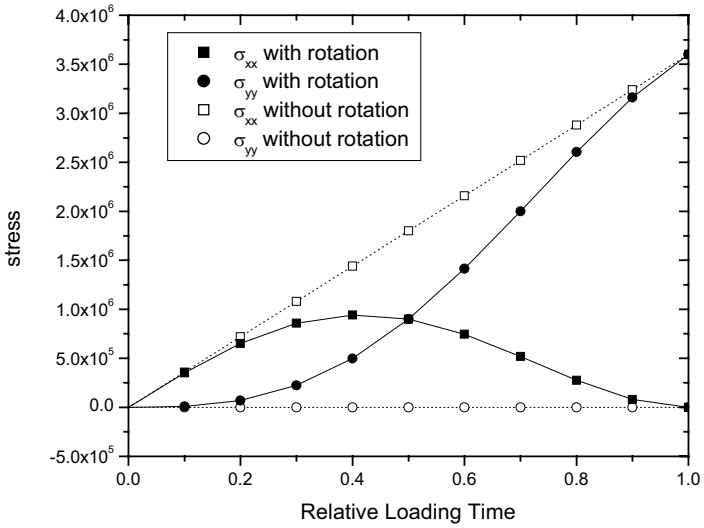

Figure 4 : The stress components of the beam under uniaxial stretch and rotation

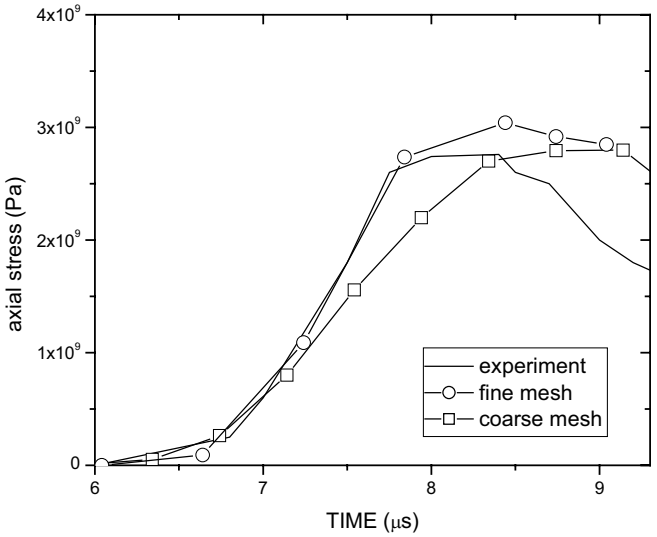

Figure 7 : Axial stress history in the rod-on-rod impact

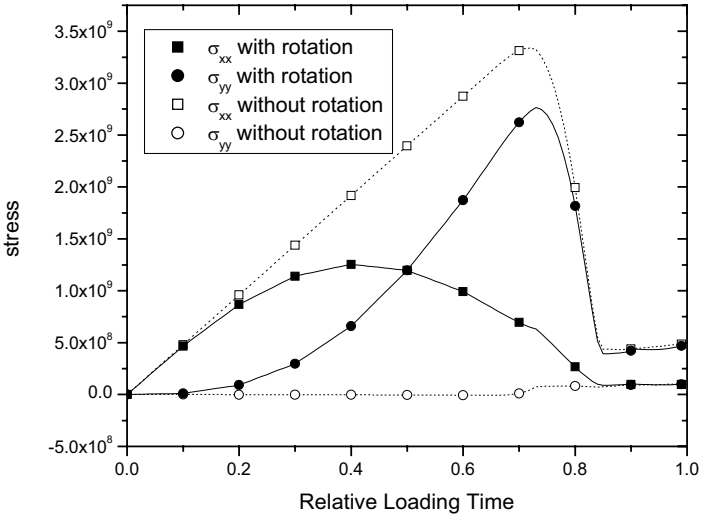

Figure 5 : The stress components of the beam under uniaxial stretch and rotation with micro-crack damage evolution

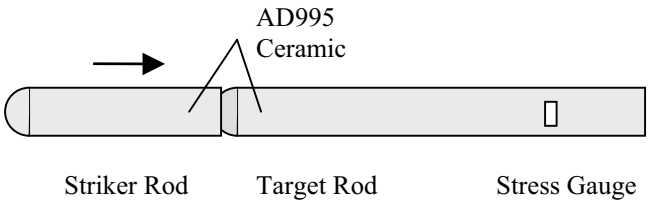

Figure 6 : Rod-on-rod impact test configuration schematic

To demonstrate the consistency of the RG model in dealing with large deformation problems, a rigid body rotation in z-direction is added to the beam. The rotation rate is set such that the beam will rotate a 90 degree in z-direction after the simulation. The stretching and rotation are applied slowly so that there is no inertia effect and a quasi-static state is maintained. The Poisson's ratio is set to be zero during the simulations.

Figure 4 shows elastic stress response obtained with RG model. The beam orientation rotates 90 degree with the uniaxial stretching, and therefore the stress tensors are rotated correspondingly. Figure 5 shows the same problem solved using RG model with micro-crack damage evolution. With the increase of the uniaxial stretching, the micro-crack opening is activated when the strain energy release rate goes beyond the critical energy release rate. The stress drops due to the micro-crack damage evolution.

4.2 Rod-on-Rod Impact

Recently, Simha (1998) conducted rod-on-rod impact experiments at the impact velocity of 278 m/s, in which both the striker and the target rods were made of AD995 ceramic. The striker rod was 5 cm long and 1.25 cm in diameter, while the target rod was 10 cm long and 1.25 cm in diameter. A stress gauge was embedded in the target rod at the location of 2.5 cm from the free end to record the axial stress history. Figure 6 shows the test configu-

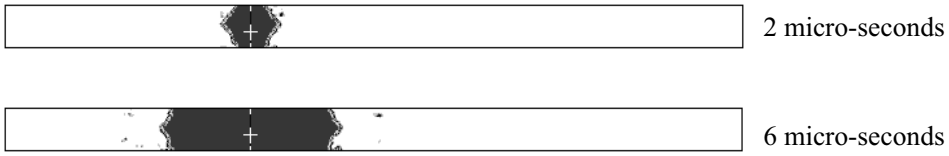

Figure 8 : Crack density profile in the rod-on-rod impact

ration. In this experiment, fracture initiates at the impact end and propagates toward the gauge location. The measured peak stress from this experiment can be used in a qualitative sense to validate the model constants under uniaxial stress.

The same problem is simulated using Dyna3D with the RG ceramic damage model. Three-dimensional finite element mesh is constructed and a quarter of the striker and target rods are modeled by considering the configuration symmetry. 49499 nodes and 254021 Tet4 elements with the average nodal spacing of 0.5 mm are used in the finite element model. The initial crack size is reduced to $a_0 = 2.3\mu m$ to avoid premature crack extension and catch the peak stress recorded in the experiment. Figure 7 compares the computed axial stress at the gauge location with the experimental data and a good agreement is obtained. A coarse mesh with average nodal spacing of 1 mm is used to re-simulate the same problem and the result is shown in Figure 7. The calculated stress from the coarse mesh increases slower than the one obtained with fine mesh, due to the loss of the high-frequency wave information of the stress wave. Figure 8 shows the micro-crack density profile, with the darkness scales of the micro-crack density. The micro-cracks begin to extend at the impact ends upon the collision of the striker and target rods. With the propagation of the stress wave, the micro-crack damage extends toward the free ends.

4.3 Plate-on-Plate Impact

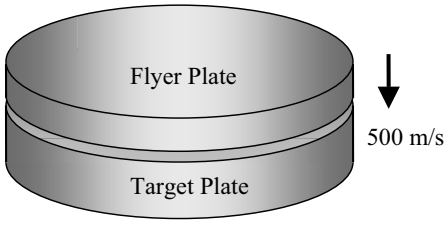

Figure 9 : Plate-on-plate impact test configuration schematic

In the simulated plate impact problem, two thin ceramic plates collide at the velocity of 500 m/s (see Figure 9). The flyer and target plates have the same diameter of 50 mm and their thicknesses are 4 mm and 8 mm, respectively. Frictionless contact is assumed between the two plates. Both the flyer and the target plates are made of AD995 ceramic.

To simulate the described problem using the MLPG software, 32058 nodes are used with an averaged nodal spacing of 1 mm. The AD995 ceramic material is modeled using Rajendran-Grove (RG) ceramic model. The material constants for RG model are listed in Table 1. For comparison purpose, the plate impact problem is also solved, using the Dyna3D. The FEM modeling uses the same nodal arrangement, and thus, 163698 Tet4 elements are produced from these nodes.

Figure 10 reports the axial velocity profiles. In Figure 10(a), the axial velocities at the central points on the free surfaces of the flyer and target plates are drawn, respectively. The velocity of the flyer plate starts to decrease while the compressive wave initiated at the collision surface arrives at the free surface. The flyer velocity becomes positive representing the bouncing back of the flyer plate. Similarly, the free surface of the target plate begins to move when the first compressive wave arrives at around 0.6 micro-seconds. This time is twice the time taken for the wave to propagate to the flyer free surface, which reflects the fact that the target plate is twice as thick as the flyer plate. The speed changes due to the arrivals of the second wave peak can be clearly observed in the target free surface velocity profile. To investigate the momentum exchange between the flyer and target plates, the averaged axial velocities are drawn in Figure 10(b). The averaged velocity is obtained by the total momentum of the flyer or target plate, divided by the total mass of the corresponding plate. At around 1.5 micro-seconds, the momentum exchange completes, which represents the end of the collision process. The target plate attains an averaged axial velocity of 270 m/s, while the flyer plate bounces back at a velocity of 38 m/s. The ve-

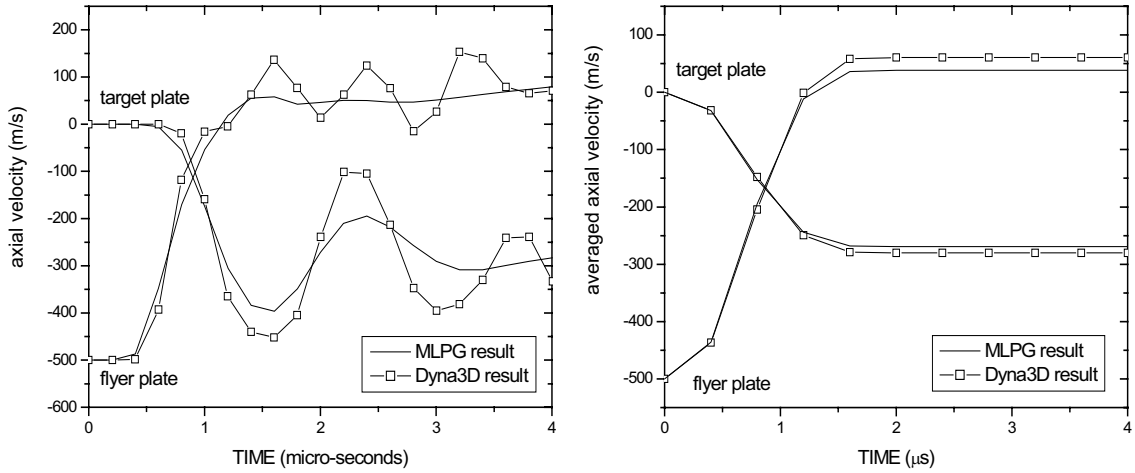

Figure 10 : (a) Axial velocities of the central points at the free surfaces of the flyer and target plates; and (b) the averaged axial velocities of the flyer and target plates

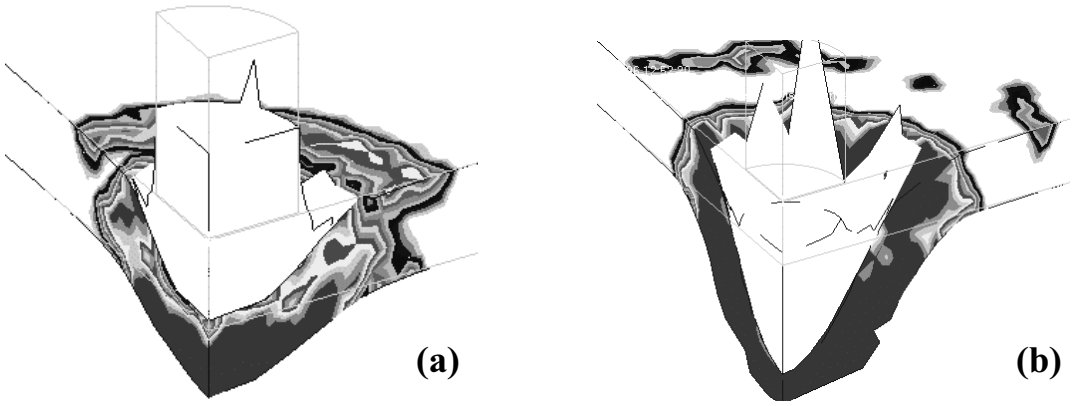

Figure 11 : Damage profiles of ballistic impact (a) 3.5 micro-seconds and (b) 10 micro-seconds

locity profiles calculated from Dyna3D are also shown in the same figures. From Figure 10(a), similar velocity histories are obtained from MLPG and Dyna3D and both of them show the same wave arrival time. The results from Dyna3D simulation are more oscillatory than the ones from MLPG. It shows that MLPG is able to obtain more stable results than the FEM, even while there are no hourglass control or other artificial "fixes" involved in the MLPG calculation. The averaged axial velocities computed from Dyna3D are shown in Figure 10(b). From this figure, it is seen that both the MLPG and Dyna3D results strictly follow the conservation of momentum. Although the Dyna3D calculation shows larger velocities for both flyer and target plates after the contact, the difference of the averaged velocities from MLPG and Dyna3D is insignificant.

4.4 Ballistic Impact

To demonstrate the capacity of the RG model on simulating the damage and penetration problems, a ballistic impact problem is considered here. In this simulation, a cylindrical tungsten projectile impacts with an AD85 ceramic plate at the velocity of 1500 m/s. Both the length and diameter of the projectile are 10 mm. The target ceramic plate has a thickness of 5 mm and a diameter of 80 mm. The tungsten is modeled as elastoplastic with the following material properties: density 16.98 g/cm^3, Young's modulus 299.6 GPa, Possion's ratio 0.21 and yield strength 1.5 GPa. The target plate is modeled using the Rajendran-Grove ceramic model, with the material constants as listed in Table 1.

This problem is simulated using both the Dyna3D and the MLPG. Figure 11 shows the damage profile from

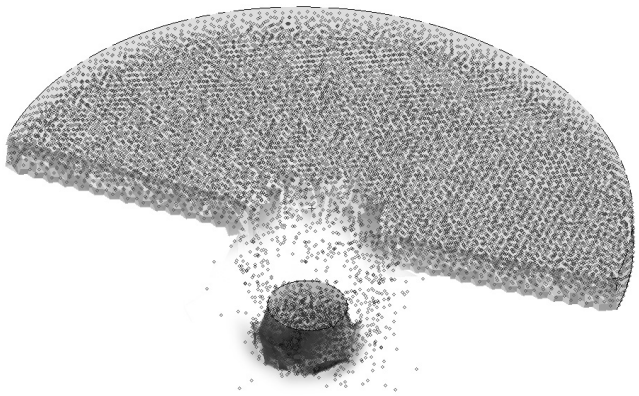

Figure 12 : Ballistic impact penetration

Dyna3D simulation, with the darkness referring to the damage density. At 3.5 micro-seconds, damage begins to form under and around the impact area. Inside these areas, the compressive stress or shear stress increases rapidly due to the collision, causing the strain energy release rate to go beyond the critical strain energy release rate. Thus, the micro-cracks begin to growth inside these areas. At 10 micro-seconds, these micro-cracks inside the whole impact area grow and cause the damage to accumulate very rapidly inside the whole impact area, to form a perforation hole. Due the incapability of the element-based method in dealing with severe distortion, the Dyna3D simulation stops at the 10 micro-seconds.

The same problem is re-simulated by using the MLPG method. The problem has been solved smoothly without any mesh distortion problems, because of the advantages of the truly meshless method. The whole penetration process is simulated and the total solution time is 20 micro-seconds. The final deformation is shown in Figure 12, and the fragmentation is clearly formed after the projectile penetrates the target plate. The detailed simulation results and discussion is reported in the author another paper [Han, Liu, Rajendran, and Atluri, (2006)].

5 Closing Remarks

The ability and accuracy of the constitutive model plays an important role in the computational methodology. The Rajendran-Grove ceramic damage model is capable of predicting the micro-crack and void damage evolution, and the pulverization of ceramic materials. The MLPG method, as a truly meshless approach, enables a feasible computational framework for solving high-speed dynamic problems with large deformation. The current mixed method, as an extension to the primal MLPG method, leads to a high-performance computational code, which can solve three-dimensional high-speed impact and penetration problems. The numerical examples demonstrate the capability of the MLPG method with RG ceramic damage model in solving the important class of impact and penetration problems, involving severe material deformation and fragmentation.

References

Atluri, S.N (2004): *The Meshless Local Petrov-Galerkin (MLPG) Method for Domain & Boundary Discretizations*, Tech Science Press, 665 pages.

Atluri, S. N.; Zhu, T. (1998): A new meshless local Petrov-Galerkin (MLPG) approach in computational mechanics. *Computational Mechanics*, Vol. 22, pp. 117-127.

Budiansky, B.; O'Connell, R.J. (1976): Elastic Moduli of Cracked Solid. *Int. J. Solids Structures*, Vol. 12, pp. 81-97.

Griffith, A.A. (1920): The Phenomena of Rupture and Flow in Solids. *Phil. Trans. R. Soc. London*, Vol. 221, pp. 163-198.

Grove, D.J. (1993): Research Report UDR-TR-93-133, University of Dayton Research Institute.

Grady, D.E.; Moody, R.L. (1996): Shock Compression Profiles in Ceramics. *Sandia Report, SADN96-0551*, Sandia National Laboratory, Albuquerque, NM.

Gurson, A.L. (1977): Porous Rigid-Plastic Materials Containing Rigid Inclusions-Yield Function, Plastic Potential and Void Nucleation. In *Adv. Res. Strength Fract. Mattls. 2a (edited by Tablin DMR)*, Pergamon Press, New York.

Han. Z. D.; Atluri, S. N. (2004): Meshless Local Petrov-Galerkin (MLPG) approaches for solving 3D Problems in elasto-statics, *CMES: Computer Modeling in Engineering & Sciences*, vol. 6 no. 2, pp. 169-188.

Han Z. D.; Rajendran, A. M; Atluri, S. N. (2005): Meshless Local Petrov-Galerkin (MLPG) Approaches for Solving Nonlinear Problems with Large Deformation and Rotation, *CMES: Computer Modeling in Engineering & Sciences*, vol. 10, no. 1, pp. 1-12.

Han Z. D.; Liu H. T.; Rajendran, A. M; Atluri, S. N. (2006): The Applications of Meshless Local Petrov-

Galerkin (MLPG) Approaches in High-Speed Impact, Penetration and Perforation Problems, *CMES: Computer Modeling in Engineering & Sciences*, vol. 14, no. 2, pp. 119-128.

Johnson, G.R.; Robert, A.S. (2003): Conversion of 3D Distorted Element into Meshless Particles During Dynamic Deformation. *Int. J. Impact Engng.*, Vol. 28, 947-966.

Margolin, L.G. (1983): Elastic Moduli of Cracked Body. *Int. J. Fract.*, Vol. 22, pp. 65-79.

Rajendran, A.M. (1994): Modeling the Impact Behavior of AD85 Ceramic under Multiaxial Loading. *Int. J. Impact Engng.*, Vol. 15, No. 3, pp. 749-768.

Rajendran, A. M.; Grove, D.J. (1996): Modeling the Shock Response of Silicon Carbide, Boron Carbide and Titanium Diboride. *Int. J. Impact Engng.,* Vol. 18, No. 6, pp. 611-631.

Rajendran, A.M.; Grove, D.J. (2002): Computational Modeling of Shock and Impact Response of Alumina. *CMES: Computer Modeling & Engng. Sci.*, Vol. 3, No. 3, 367-380.

Resnyansk, A.D. (2002): DYNA-Modeling of the High-Velocity Impact Problems with a Split-Element Algorithm, *Int. J. Impact Engng.*, Vol. 27, 709-727.

Simha, C.H.M. (1998): High Rate Loading of a High Purity Ceramic – One Dimensional Stress Experiments and Constitutive Modeling. Ph.D. thesis, University of Texas, Austin, Texas.